AGU PUBLICATIONS

Global Biogeochemical Cycles

RESEARCH ARTICLE
10.1002/2013GB004704

Key Points:
- The triple oxygen isotope tracer system was added to global ocean model
- Model results evaluated against all available triple oxygen isotope data
- Biases in steady state equation for production quantified

Supporting Information:
- Readme
- Figure S1
- Equations (S1)–(S9) and Figure S1

Correspondence to:
D. Nicholson,
dnicholson@whoi.edu

Citation:
Nicholson, D., R. H. R. Stanley, and S. C. Doney (2014), The triple oxygen isotope tracer of primary productivity in a dynamic ocean model, *Global Biogeochem. Cycles*, *28*, 538–552, doi:10.1002/2013GB004704.

Received 30 JUL 2013
Accepted 21 APR 2014
Accepted article online 29 APR 2014
Published online 23 MAY 2013

The triple oxygen isotope tracer of primary productivity in a dynamic ocean model

David Nicholson[1], Rachel H. R. Stanley[1], and Scott C. Doney[1]

[1]Department of Marine Chemistry and Geochemistry, Woods Hole Oceanographic Institution, Woods Hole, Massachusetts, USA

Abstract The triple oxygen isotopic composition of dissolved oxygen ($^{17}\Delta_{dis}$) was added to the ocean ecosystem and biogeochemistry component of the Community Earth System Model, version 1.1.1. Model simulations were used to investigate the biological and physical dynamics of $^{17}\Delta_{dis}$ and assess its application as a tracer of gross photosynthetic production (gross oxygen production (*GOP*)) of O_2 in the ocean mixed layer. The model reproduced large-scale patterns of $^{17}\Delta_{dis}$ found in observational data across diverse biogeographical provinces. Mixed layer model performance was best in the Pacific and had a negative bias in the North Atlantic and a positive bias in the Southern Ocean. Based on model results, the steady state equation commonly used to calculate GOP from tracer values overestimated the globally averaged model GOP by 29%. Vertical entrainment/mixing and the time rate of change of $^{17}\Delta_{dis}$ were the two largest sources of bias when applying the steady state method to calculate GOP. Entrainment/mixing resulted in the largest overestimation in midlatitudes and during summer and fall and almost never caused an underestimation of GOP. The tracer time rate of change bias resulted both in underestimation of GOP (e.g., during spring blooms at high latitudes) and overestimation (e.g., during the summer following a bloom). Seasonally, bias was highest in the fall (September-October-November in the Northern Hemisphere, March-April-May in the Southern), overestimating GOP by 62%, globally averaged. Overall, the steady state method was most accurate in equatorial and low-latitude regions where it estimated GOP to within ±10%. Field applicable correction terms are derived for entrainment and mixing that capture 86% of model vertical bias and require only mixed layer depth history and triple oxygen isotope measurements from two depths.

1. Introduction

Photosynthesis in the upper ocean plays a critical role in the global biogeochemical cycling of carbon and oxygen and provides the energy and organic carbon that support the great majority of ocean ecosystems. Accurate assessment of the metabolic rates of ecosystems in the upper ocean is thus a central challenge to understanding biogeochemical fluxes and their controls in the marine environment.

The triple oxygen isotopic (TOI) composition of dissolved oxygen has, over the last decade, become widely adopted as a powerful new tracer of upper ocean biological productivity. The TOI composition of the mixed layer provides an estimate of gross photosynthetic production (GPP) [*Juranek and Quay*, 2013; *Luz and Barkan*, 2000]. As the term GPP can refer to carbon, oxygen, or even energy fluxes, we use *GOP* to refer specifically to the gross production of O_2, the quantity determined by the TOI method. As a productivity tracer, TOI has a number of distinct advantages. It measures a natural, in situ quantity and thus has the advantage of not requiring isotope labeling and associated incubation and sampling artifacts. This enables the collection of large amounts of data using improved measurement capabilities including underway collection of TOI samples, including from ships of opportunity [*Juranek and Quay*, 2010; *Reuer et al.*, 2007]. Subsequently, TOI observations have proliferated and span all major ocean basins and many coastal zones, although many results have yet to be published [*Juranek and Quay*, 2013].

The vast majority of TOI observations have been collected in the mixed layer of the ocean. Interpreting mixed layer TOI signatures in terms of a rate of productivity requires assumptions be made about mixed layer and biological dynamics. Generally, the TOI system is interpreted assuming a steady state mixed layer (i.e., tracer values are not changing with time) and no transport fluxes (i.e., no entrainment, mixing, or advective fluxes). Studies have demonstrated that both the steady state assumption [*Hamme et al.*, 2012] and transport assumption [*Nicholson et al.*, 2012] can cause large biases in calculated productivity rates. For example, the thermocline often has an enriched TOI ^{17}O excess signal which is introduced into the mixed layer during seasonal fall entrainment and causes an overestimate of GOP [*Nicholson et al.*, 2012]. The magnitude of such

potential biases is expected to vary both in space and in time yet has been evaluated only to a limited degree in a handful of locales. Not only do biases impact individual estimates of GOP, depending on the spatiotemporal scale of biases, the ability to accurately determine seasonal cycles and spatial gradients of GOP will be adversely affected as well. Here we present an assessment of the TOI tracer system on a global scale.

We have added oxygen isotopes to a global ocean model, the Parallel Ocean Program (POP) of the Community Earth System Model version 1.1.1 (CESM-1) [*Danabasoglu et al.*, 2012; *Gent et al.*, 2011], to elucidate the behavior of this tracer system in a dynamical context and to evaluate systematic biases in applying TOI to estimate GOP. Many of the large-scale patterns of global circulation that help define oceanic biomes cause predictable and systematic biases in TOI-based productivity estimates. Accounting for biases introduced by the dynamic behavior of the TOI system is a crucial step in reaching the full potential of the tracer as a measure of global rates and patterns of ocean productivity. Toward this end, we have applied our insights from numerical modeling exercises to identify spatiotemporal patterns in physical biases in estimating GOP. Understanding and accounting for such biases will enable improved characterization of large-scale patterns in ocean productivity via the TOI tracer system.

2. The Triple Oxygen Isotope System

2.1. Mass Balance Equations

The TOI approach combines observations of the $^{18}\delta$ and $^{17}\delta$ isotopic ratios of dissolved oxygen with a conceptual mixed layer box model to calculate GPP by mass balance. Delta notation used herein refers to the isotopic composition of oxygen with respect to atmospheric air standard such that follows:

$$^{*}\delta = 10^{3}\left(\frac{\left(^{*}\mathrm{O}/^{16}\mathrm{O}\right)_{\mathrm{sample}}}{\left(^{*}\mathrm{O}/^{16}\mathrm{O}\right)_{\mathrm{std}}} - 1\right) \quad \text{where "*" refers to 17 or 18} \tag{1}$$

The usefulness of combining $^{18}\delta$ and $^{17}\delta$ depends on the fact that atmospheric dissolved oxygen has a mass independent depletion of $^{17}\delta$ relative to $^{18}\delta$ due to processes in the stratosphere [*Lämmerzahl et al.*, 2002; *Luz and Barkan*, 2000]. Thus, dissolved oxygen produced photosynthetically from water molecules in the mixed layer contains excess ^{17}O relative to atmospherically derived oxygen, a signature which can be used to diagnose photosynthetic rates. Respiration alters both $^{18}\delta$ and $^{17}\delta$, but in a known, mass-dependent manner, and the effects of respiration can largely be canceled out using a mass-dependent fractionation slope, λ. For visualizing the combined information of $^{18}\delta$ and $^{17}\delta$, it is useful to define a single tracer, $^{17}\Delta$:

$$^{17}\Delta \equiv 10^{6}\left[\log\left(1+\frac{^{17}\delta}{10^{3}}\right) - \lambda \log\left(1+\frac{^{18}\delta}{10^{3}}\right)\right] \tag{2}$$

where $\lambda = \gamma_R = 0.518$, which is the experimentally determined ratio of fractionation factors during ordinary respiration ($^{17}\varepsilon_R/^{18}\varepsilon_R$) [*Angert et al.*, 2003; *Helman et al.*, 2005; *Luz and Barkan*, 2005]. Observed mixed layer ^{17}O excess ($^{17}\Delta_{\mathrm{dis}}$) falls between the photosynthetic end-member ($^{17}\Delta_P \approx 249$ ppm) and the atmospheric equilibrium end-member ($^{17}\Delta_{\mathrm{eq}} \approx 8$ ppm).

Recently, improved equations have been proposed for calculating GOP from TOI mass balance equations for ^{16}O, ^{17}O, and ^{18}O using the "dual delta" approach [*Kaiser*, 2011; *Prokopenko et al.*, 2011]. The following is from equation (6) from *Prokopenko et al.* [2011]:

$$z_{\mathrm{ml}}[\mathrm{O}_2]\frac{\mathrm{d}(^{17}\Delta_{\mathrm{dis}})}{\mathrm{d}t} = P_{\mathrm{ml}}A_P - k[\mathrm{O}_2]_{\mathrm{eq}}A_{\mathrm{eq}} \tag{3}$$

where P_{ml} is mixed layer GOP (mol $\mathrm{O}_2\,\mathrm{m}^{-2}\,\mathrm{d}^{-1}$), $[\mathrm{O}_2]$ and $[\mathrm{O}_2]_{\mathrm{eq}}$ are observed and equilibrium oxygen concentration [*Garcia and Gordon*, 1992] of the mixed layer (mol $\mathrm{O}_2\,\mathrm{m}^{-3}$), k is the gas transfer coefficient ($\mathrm{m\,s}^{-1}$), z_{ml} (m) is the mixed layer depth, and the abbreviation "A_x" is defined as follows:

$$A_x \equiv \frac{\left(^{17}\mathrm{O}/^{16}\mathrm{O}\right)_x - \left(^{17}\mathrm{O}/^{16}\mathrm{O}\right)_{\mathrm{dis}}}{\left(^{17}\mathrm{O}/^{16}\mathrm{O}\right)_{\mathrm{dis}}} - \gamma_R\frac{\left(^{18}\mathrm{O}/^{16}\mathrm{O}\right)_x - \left(^{18}\mathrm{O}/^{16}\mathrm{O}\right)_{\mathrm{dis}}}{\left(^{18}\mathrm{O}/^{16}\mathrm{O}\right)_{\mathrm{dis}}} \tag{4}$$

and the subscripts "P" and "eq" refer to the photosynthetic and atmospheric equilibrium end-members, respectively. In equation (3), the left side of the equation is the mixed layer integrated time rate of change, which is determined by the two terms on the right for photosynthetic production and air-sea gas exchange.

The above equation (equation (3)) omits minor terms for the effects of kinetic fractionation during gas exchange and air-sea bubble flux processes [*Kaiser*, 2011; *Nicholson et al.*, 2012]. Bubble fluxes are not represented in the model, but mass-dependent differences in isotopologue diffusivity and thus kinetic fractionation are included. Generally, GOP has been calculated by assuming the time rate of change term (left side of equation (3)) is small and can be neglected. If so, the equation simplifies to the steady state solution

$$P_{\mathrm{ml}} = k[\mathrm{O_2}]_{\mathrm{eq}} \frac{A_{\mathrm{eq}}}{A_P} \tag{5}$$

2.2. Beyond the Steady State Assumption

The equation used to calculate GOP (equation (5)) is derived from the assumption of a fixed-depth mixed layer in isotopic steady state with the atmosphere through air-sea gas exchange. Additionally, the equations assume that lateral advective fluxes and vertical entrainment and advection do not influence the time rate of change of $^{17}\Delta_{\mathrm{dis}}$. Recent studies, however, suggest that assuming steady state when calculating GOP may introduce significant error and bias under a wide range of physical conditions [*Hamme et al.*, 2012; *Nicholson et al.*, 2012]. When such assumptions clearly are violated, such as in active upwelling regions, or during fall entrainment, investigators, aware of such concerns, have often chosen either not to attempt to interpret their tracer data, or heavily caveat their interpretation of the results from these periods. Our modeling approach, which includes a number of diagnostic outputs, allows for the assessment of the nonsteady state terms of equation (3). By adding the TOI system to a global ocean model, we assessed the role of physical circulation and nonsteady state dynamics in biasing estimates of GOP. Insights from model results can be applied to improve estimates of GOP from field TOI observations.

3. Methods

3.1. Model Implementation

We have simulated the distribution of the TOI tracer system in the Parallel Ocean Program (POP), the 3-D global ocean component of the Community Earth System Model version 1.1.1 (CESM-1) [*Danabasoglu et al.*, 2012; *Gent et al.*, 2011]. The model was run at a nominal 1° by 1° resolution with 60 vertical levels [*Danabasoglu et al.*, 2012]. Vertical spacing is 10 m in the upper 160 m. Vertical mixing in POP is implemented using the K-profile parameterization [*Large et al.*, 1994] which includes both local and nonlocal mixing terms and a constant background diffusivity ($1 \times 10^{-5}\,\mathrm{m^2\,s^{-1}}$) [*Danabasoglu et al.*, 2012]. Mixing is strongly enhanced over a surface planetary boundary layer, *h*, which is determined based on bulk Richardson number. Boundary layer mixing is strongly influenced by surface buoyancy and momentum forcing. Because *h* can extend below the mixed layer depth (if defined strictly by vertical stratification), a fraction of boundary layer mixing enhances communication between the mixed layer and thermocline [*Danabasoglu et al.*, 2012; *Large et al.*, 1994]. Gas tracers were added to the Biogeochemical Elemental Cycling (BEC) model component, which includes an upper ocean ecosystem module [*Moore et al.*, 2004] and full-depth biogeochemistry module [*Doney et al.*, 2006; *Long et al.*, 2013; *Moore et al.*, 2013]. The ocean model is forced with satellite data products [*Doney et al.*, 2007] and a time-varying dust deposition. Model performance has been evaluated over a multidecadal hindcast simulation against field and satellite observations for CESM-1 [*Moore et al.*, 2013] as well as for its predecessor, CCSM-3 [*Doney et al.*, 2009]. For CESM-1 seasonally varying mixed layer depth is generally within 10 m of observations although with a shallow bias in the Southern Ocean. Surface nutrients and chlorophyll have a positive bias at low latitudes and negative bias at high latitudes, and the volume of subsurface oxygen deficient zones is overestimated [*Moore et al.*, 2013]. Anthropogenic carbon uptake on interannual to decadal scales is reasonably well represented, although there is a positive bias in uptake in the North Atlantic and negative bias in the Southern Ocean [*Long et al.*, 2013].

Three functional phytoplankton types, large (micro)phytoplankton, small (pico/nano)phytoplankton, and diazatrophs, contribute to model photosynthesis, which, in the standard version of the model, is calculated in terms of net carbon growth rate (gross photosynthesis minus autotrophic respiration) [*Moore et al.*, 2004]. Heterotrophic respiration in the model is also in carbon units and is represented in terms of grazing by a single adaptive zooplankton class, nongrazing mortality, and remineralization of particulate and dissolved organic carbon.

To the standard configuration of the BEC component of CESM, we have added a tracer for the oxygen isotopomers $^{33}O_2$ and $^{34}O_2$ in addition to the dominant $^{32}O_2$ form. The sources and sinks of these passive

tracers include gas exchange with the atmosphere at the air-sea interface and production and consumption by gross photosynthesis and total respiration, respectively. The magnitude of each flux is related to O_2 fluxes by fractionation factors associated with each process in addition to the dissolved isotopic ratios [*Nicholson et al.*, 2012]. Biological fractionation is determined from the ecosystem model-determined rates of photosynthetic oxygen production (P) and respiratory oxygen consumption (R) such that

$$\frac{\partial([O_2]_{dis}\,{}^{*}r_{dis})}{\partial t} = P\,{}^{*}r_P - R\,{}^{*}\alpha_R\,{}^{*}r_{dis} \tag{6}$$

where * refers to either 18 or 17, ${}^{*}r_P$ is the ${}^{*}O/{}^{16}O$ ratio of photosynthetically produced O_2 [*Luz and Barkan*, 2011], ${}^{*}r_{dis}$ is the ${}^{*}O/{}^{16}O$ ratio of dissolved oxygen, and ${}^{*}\alpha_R$ is the fractionation factor during respiration. The BEC model only includes net primary production of oxygen (NPP^{O2}) (rather than gross), so we chose to apply a conversion factor of 2.3 to NPP^{O2} to derive GOP. The model already includes a NPP^{O2} to NPP^{C} photosynthetic quotient of 1.45 for nitrate based photosynthesis and 1.18 for recycled/ammonia based productivity and 1.28 for diazotrophic production. The GOP:NPP^{O2} value 2.3 was chosen so as to result in GOP:NPP^{C} ratios of 3.3, 3.0, and 2.7 for nitrate-, ammonia-, and diazotrophic-driven productivity, respectively. These ratios are consistent with a recent laboratory study showing a ratio of 3.3 for a diatom grown on nitrate [*Halsey et al.*, 2010] as well as field-based incubation studies which averaged 2.7, presumably when recycled productivity was on average more prevalent [*Laws et al.*, 2000; *Marra*, 2002]. Whether GOP:NPP^{O2} varies significantly and coherently across ocean biomes is not well understood [*Juranek and Quay*, 2013], and our assumption of a fixed GOP:NPP^{O2} does not represent such dynamics.

To complete the biological oxygen budget we increase model respiration rate by adding autotrophic respiration ($GOP - NPP^{O2}$) to preexisting heterotrophic respiration. Gas exchange for ${}^{*}O$ includes equilibrium (${}^{*}\alpha_{eq}$) and kinetic fractionation (${}^{*}\alpha_{gek}$) corrections based on measured values [*Benson and Krause*, 1984; *Knox et al.*, 1992; *Luz and Barkan*, 2009]. The air-sea flux equation is

$${}^{*}F_{ge} = -{}^{*}\alpha_{gek} f_{ice} k_{O_2}\left({}^{*}r_{dis}[O_2]_{dis} - \frac{p_{slp} - p_w}{p_{atm} - p_w}\left({}^{*}\alpha_{eq}\,{}^{*}r_{atm}[O_2]_{eq}\right)\right) \tag{7}$$

where f_{ice} is fractional ice coverage; k_{O2} is the gas transfer coefficient for O_2 at in situ temperature; and p_{slp}, p_{atm}, and p_w. are the observed sea level pressure, standard atmospheric pressure, and the saturated water vapor pressure, respectively.

In practice, the TOI system was implemented by adding two tracers in addition to O_2, which allows for simulation of the TOI system with improved numerical performance. The first tracer, termed ${}^{18}O_{xs}$ is related to ${}^{18}\delta_{dis}$ and defined as follows:

$${}^{18}O_{xs} = [O_2]_{dis}\left(\frac{{}^{18}\delta_{dis}}{10^3}\right) \tag{8}$$

where the subscript dis refers to the composition of dissolved oxygen. The tracer is closely related to ${}^{18}\delta$ but conserves mass. Note that following convention, all delta values refer to atmospheric O_2 (subscript atm) as the reference material. The ${}^{17}O_{xs}$ tracer is defined to also conserve mass and to be closely related to ${}^{17}\Delta_{dis}$ in that the effects of respiration largely cancel.

$${}^{17}O_{xs} = [O_2]_{dis}\left(\frac{{}^{17}\delta_{dis} - \gamma_R\,{}^{18}\delta_{dis}}{10^3}\right) \tag{9}$$

When ${}^{18}\delta_{dis}$ is small (e.g., as usually is the case in the mixed layer), ${}^{17}O_{xs}/O_{dis} \approx {}^{17}\Delta_{dis}$. The decomposition of the TOI system into conservative tracers including one closely related to ${}^{17}\Delta_{dis}$ not only improves numerical performance but also makes it much easier to calculate diagnostic flux tendencies due to physical circulation (see section 5.2).

The model was initialized with ${}^{18}\delta_{dis} = 0‰$ and ${}^{17}\Delta_{dis} = 40$ ppm based on 2000 m observations near Bermuda [*Luz and Barkan*, 2009]. Final results and conclusions were not sensitive to reasonable changes in the choice of deep ocean initial conditions. The model was spun up for 200 years with a repeating climatological normal year forcing which was sufficient time for the evolution of mixed layer and thermocline dynamics to an approximate dynamically consistent steady state. No interannual drift in mixed layer or thermocline ${}^{17}\Delta_{dis}$ was evident after

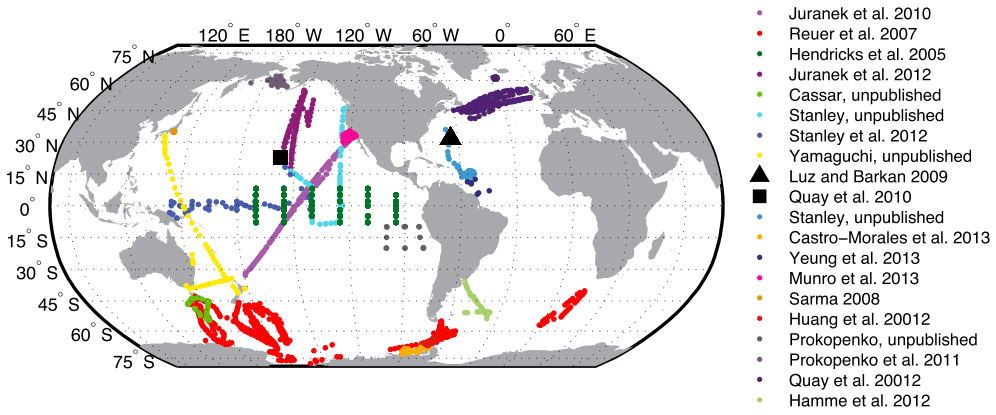

Figure 1. Locations of sample data. Large black symbols indicate annual time series locations.

the 200 year spin-up. Following spin-up, a hindcast simulation with interannual variability was performed for the period 1966–2009. The hindcast experiment was used to directly compare model results to field observations and to assess if the model could capture interannual variability in dissolved gas tracers.

3.2. Observational Data

We include data from 20 studies with a total of 2730 $^{17}\Delta_{dis}$ observations, 2192 of which were in the mixed layer (Figure 1). Six of these studies were restricted to the coastal regions ($n = 434$) of the California Margin [*Munro et al.*, 2013], Sagami Bay, Japan [*Sarma et al.*, 2008], Bering Sea [*Prokopenko et al.*, 2011], Bellingshaus Sea [*Castro-Morales et al.*, 2012], Antarctic Peninsula [*Huang et al.*, 2012], and Amazon outflow [*Yeung et al.*, 2012]. We include eight open ocean Pacific data sets ($n = 797$) with two in the equatorial Pacific [*Hendricks et al.*, 2005; *Stanley et al.*, 2010], four spanning large transects [*Juranek and Quay*, 2010; *Juranek et al.*, 2012; R. H. R. Stanley, unpublished data, 2007; H. Yamagishi, unpublished data, 2008], one in the eastern south tropical Pacific (Prokopenko et al., unpublished data), one at the Hawaii Ocean Timeseries (HOT) subtropical time series [*Quay et al.*, 2010], three studies in open Southern Ocean ($n = 582$) [*Hamme et al.*, 2012; *Reuer et al.*, 2007; Cassar et al., submitted manuscript], and three from the open Atlantic ($n = 379$) [*Luz and Barkan*, 2009; *Quay et al.*, 2012; Stanley et al, submitted manuscript]. Because a number of studies did not report both $^{18}\delta$ and $^{17}\delta$ directly and used slightly different definitions for $^{17}\Delta_{dis}$ and different values for $^{17}\Delta_{eq}$ [*Luz and Barkan*, 2009; *Stanley et al.*, 2010], we recalculated $^{17}\delta$ and $^{17}\Delta_{dis}$ to be consistent with the definition for $^{17}\Delta$ used here (equation (2)). Unfortunately, we were unable to obtain consistent and complete records for wind speed, weighted gas transfer coefficient, dissolved oxygen, and mixed layer depth across the studies. We suggest that future studies publish as full a set of ancillary data as possible to enhance intercomparability.

4. Results and Discussion: Simulated $^{17}\Delta_{dis}$ and Comparison to Field Data

4.1. Mixed Layer $^{17}\Delta_{dis}$

The climatological seasonal cycle of mixed layer $^{17}\Delta_{dis}$ after spin-up was dictated by regional patterns of biological activity, wind variability, and ocean physics (Figure 2). Higher values of $^{17}\Delta_{dis}$ are associated with regions and seasons of high productivity and low wind speed such as regions of equatorial upwelling (where the photosynthetic contribution to dissolved O_2 is enhanced and the atmospheric O_2 contribution reduced). High values were also evident where productivity occurred under sea ice in the Arctic and Antarctic. The model parameterized gas transfer as proportional to the ice-free fraction of the surface, so high $^{17}\Delta_{dis}$ values in areas of sea ice are due to low or absent outgassing of biologically produced O_2. As actual gas transfer may be higher than predicted by this linear model [*Loose et al.*, 2009], under-ice $^{17}\Delta_{dis}$ may be overestimated in CESM.

Observations were compared to model results directly, by matching each observation to model data from the nearest grid point, from the appropriate model monthly mean output. Observations were compared both to the normal year forcing (NYF) (mean seasonal cycle) simulation and to the hindcast simulation with interannual forcing (IAF) (Table 1). For the combined data set including all mixed layer observations of $^{17}\Delta_{dis}$ ($n = 2192$) the mean value

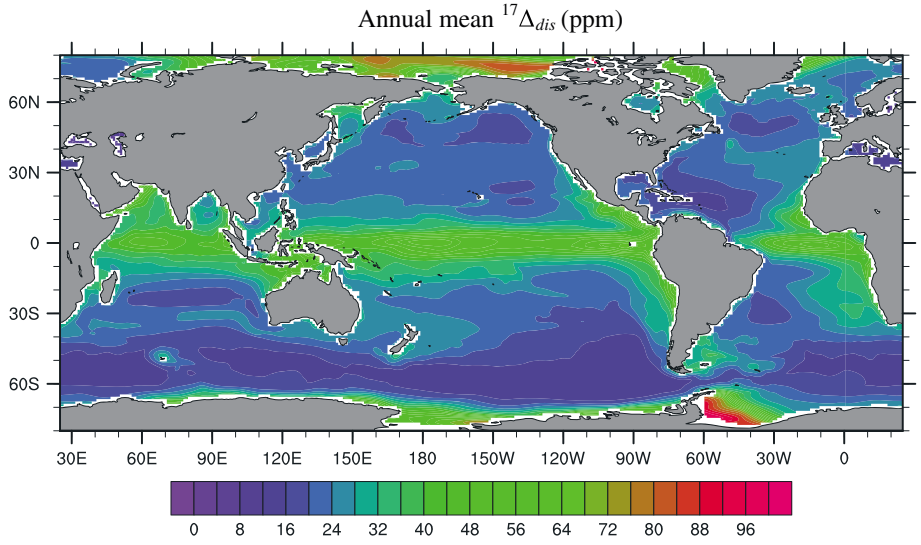

Figure 2. Annual mean mixed layer $^{17}\Delta_{dis}$ (ppm) for normal year forcing simulation after model spin-up.

(m_{obs}) of 36.0 ppm with standard deviation $\sigma_{obs} = 19.1$. Corresponding NYF model results had a mean bias (b_{NYF}) of −5.2 ppm ($m_{NYF} = 30.8$) and a centered pattern root-mean-square difference ($RMSD_{CP}$) of 21.4 ppm where

$$RMSD_{CP} = \left(\frac{1}{n} \sum_{i=1}^{n} ((s_i - \bar{s}) - (o_i - \bar{o}))^2 \right)^{1/2} \quad (10)$$

where "*s*" denotes model values and "*o*" denotes observations. The bias of −5.2 ppm was due in large part to large biases in coastal studies for which there was a mean bias of −19.9 ppm. The model resolution likely is insufficient to capture the dynamics of highly productive coastal oceans. The interannually forced (IAF) hindcast simulation resulted in only minor improvements compared to NYF simulation (Table 1). None of the differences in $RMSD_{CP}$ were statistically significant between NYF and IAF simulations. For all mixed layer observations there was a mean bias in the IAF of −4.8, correlation was $r = 0.30$, and $RMSD_{CP}$ was 20.7. Regionally, $^{17}\Delta_{dis}$ correlation between data and NYF ranged from $r = 0.16$ in the Southern Ocean to $r = 0.66$ in the Pacific. Generally, observational data sets that spanned large geographical (and biogeochemical) ranges had higher correlation. Observational variance exceeded model variance for all data sets, likely due to the monthly averaging and approximately 1° resolution of the model.

Field observations of $^{17}\Delta_{dis}$ can vary significantly over very short distances (less than the ~1° model resolution) due to mesoscale and submesoscale dynamics not represented in the model, thus attempting to match observations to the model point-by-point presents a significant challenge. Biogeographical patterns in $^{17}\Delta_{dis}$ are more readily apparent when binning nearby observations, an approach that has been taken in observational studies [*Quay et al.*, 2012]. To this end, results we binned NYF results into biogeographic

Table 1. Statistical Summary of Data-Model Comparison for $^{17}\Delta_{dis}$[a]

	Observations	Normal Year Forcing			Interannual Forcing		
	m_{obs} (σ_{obs})	b_{NYF}	$RMSD_{CP}$	r_{NYF}	b_{IAF}	$RMSD_{CP}$	r_{IAF}
All obs. ($n = 2192$)	36.0 (19.1)	−5.2	21.4	0.28	−4.8	20.7	0.30
Open ocean ($n = 1758$)	33.1 (15.1)	−1.6	18.4	0.36	−1.8	17.8	0.36
Pacific ($n = 797$)	36.1 (16.0)	−3.3	12.2	0.66	−3.2	12.4	0.64
Atlantic ($n = 379$)	31.7 (14.1)	**−6.7**	14.4	0.43	**−9.5**	12.8	0.42
Southern ($n = 582$)	30.3 (13.6)	+4.1	25.1	0.16	+5.1	23.5	0.22
Coastal ($n = 434$)	47.7 (27.3)	**−19.9**	25.9	0.33	**−16.8**	26.3	0.29

[a]Each observation was matched to the nearest monthly mean and grid point location from model output. NYF refers to the normal year forcing simulation, and IAF refers to the interannual forcing simulation. Mean (ppm) is denoted by "*m*," "*b*" is bias (ppm), "*r*" is correlation coefficient, and $RMSD_{CP}$ is centered pattern root-mean-square difference (equation (10)) (ppm). Bold values indicated values where there was a statistically significant ($p < 0.05$) difference between NYF and IAF simulations. All correlation coefficients are statistically significant as are all biases between model and observed data.

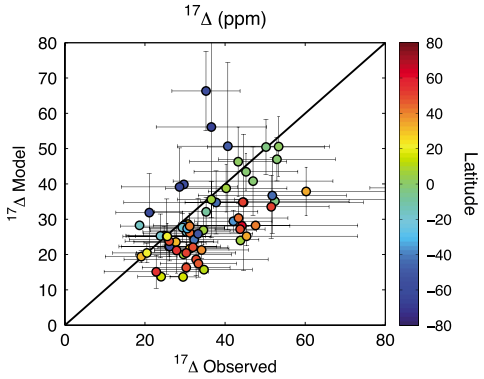

Figure 3. Mixed layer observed $^{17}\Delta$ plotted against corresponding model values. Model values are from the interannually forced simulation following a 200 year spin-up and represent monthly mean values binned by ocean province [*Longhurst*, 2006] and by seasons (winter/spring/summer/fall). Colors correspond to province latitude, with warm colors for the Northern Hemisphere, green near the equator, and cool colors in the Southern Hemisphere.

provinces [*Longhurst*, 2006] and into four seasons (December-anuary-February, March-April-May, June-July-August, and September-October-November). For each bin, model and data averages were calculated from the set of matched pairs falling within the bounds of each province. Our data set includes observations from 32 of the 54 Longhurst provinces, with an average of 2.1 seasons represented for each of 32 represented provinces. Binning data improved the correlation coefficient ($r = 0.49$), with $RMSD_{CP}$ of 11.7 ppm and bias of −6.6 ppm (Figure 3). When including data only from the 13 open ocean studies, we find a correlation of $r = 0.56$ and RMS of 9.5 ppm and bias of −3.7 ppm. Binning data significantly improved model-data comparisons across the data set, indicating that the model had better skill at representing seasonal and interregional variations than for intraregional and smaller-scale patterns.

While the expected 1:1 provides a reasonable fit, there remains significant misfit between model and observations. In particular, model results were biased high for the Southern Ocean, and low for the North Atlantic. These could be due to deficiencies in the ecosystem model, such as model error in predicting the abundance and growth rate of phytoplankton, or shortcomings in how we represent the TOI system. For example, the GOP:NPP^C ratio could vary more significantly than the very minor range permitted in our model, which employs a fixed GOP:NPP^{O2} and varies only due the impact of the type of nitrogen utilization on NPP^{O2}:NPP^C. The current understanding of what causes variations in GOP:NPP^C as well as the performance of models in accurately predicting NPP^C is as of yet not sufficient for us to distinguish between these two potential sources of error. Evaluation of CESM-BEC model performance on related parameters such as chlorophyll and nutrients [*Moore et al.*, 2013] hints at the possibility that biases in model NPP^C contribute significantly to biases in $^{17}\Delta_{dis}$. Around the Antarctic Peninsula and Southern Ocean island systems, CESM overestimates chlorophyll, likely due to the magnitude of shelf iron resuspension. Along coastal margins, such as the California margin and Amazon outflow region, CESM does not capture high levels of productivity and chlorophyll.

4.2. Thermocline $^{17}\Delta_{dis}$

Below the mixed layer, $^{17}\Delta_{dis}$ values were high where photosynthesis was active yet isolated from the influence of low $^{17}\Delta$ from the atmosphere. Values in excess of 100 ppm are present at midlatitudes at around 50–100 m in the upper thermocline in the summer (Figure 4). On average, model results in the thermocline are lower than have been observed [*Hendricks et al.*, 2005; *Luz and Barkan*, 2009; *Quay et al.*, 2010], particularly at depths below 150 m (Figure 5). A likely cause for this deficiency is that model photosynthesis is not occurring as deeply and as intensely as it should. For example, in the subtropical Pacific, near the Hawaii Ocean Timeseries (HOT), photosynthesis in the model extends no deeper than about 140 m and the deep chlorophyll maximum is no deeper than 80 m. Observations show that the deep chlorophyll maximum is around 120 m depth [*Letelier et al.*, 2004], with Prochlorococcus found in abundance down to at least 200 m [*Johnson et al.*, 2006]. Furthermore, our model does not include any photosynthetic activity below the compensation depth. A range of processes not considered by the model, such as photoheterotrophy which has been observed in cyanobacteria [*Eiler*, 2006; *Muñoz-Marín et al.*, 2013], could help account for the deficiency of deeper $^{17}\Delta$.

Below the sunlit thermocline, particularly in areas of low oxygen, $^{17}\Delta_{dis}$ becomes negative (Figure 6). Negative values occur because, while respiration alone does not alter $^{17}\Delta_{dis}$, the tracer is nonconservative when the effects of respiration and mixing are combined. This behavior can be illustrated by a simple mixing calculation between a hypothetical parcel of surface water ($O_2 = 225$ mmol m^{-3}, $^{18}\delta = 0$ per mil, and $^{17}\Delta_{dis} = 40$ ppm) and a second parcel which started with the composition of the first then underwent respiratory Rayleigh fractionation ($\alpha_R = 0.980$) until 5% of oxygen remained (($O_2 = 11.25$ mmol m^{-3}, $^{18}\delta = 61.7$ per mil, and $^{17}\Delta_{dis} = 40$ ppm)) [*Levine et al.*, 2009]. Although both end-members have equal $^{17}\Delta_{dis}$, mixing between the two results in

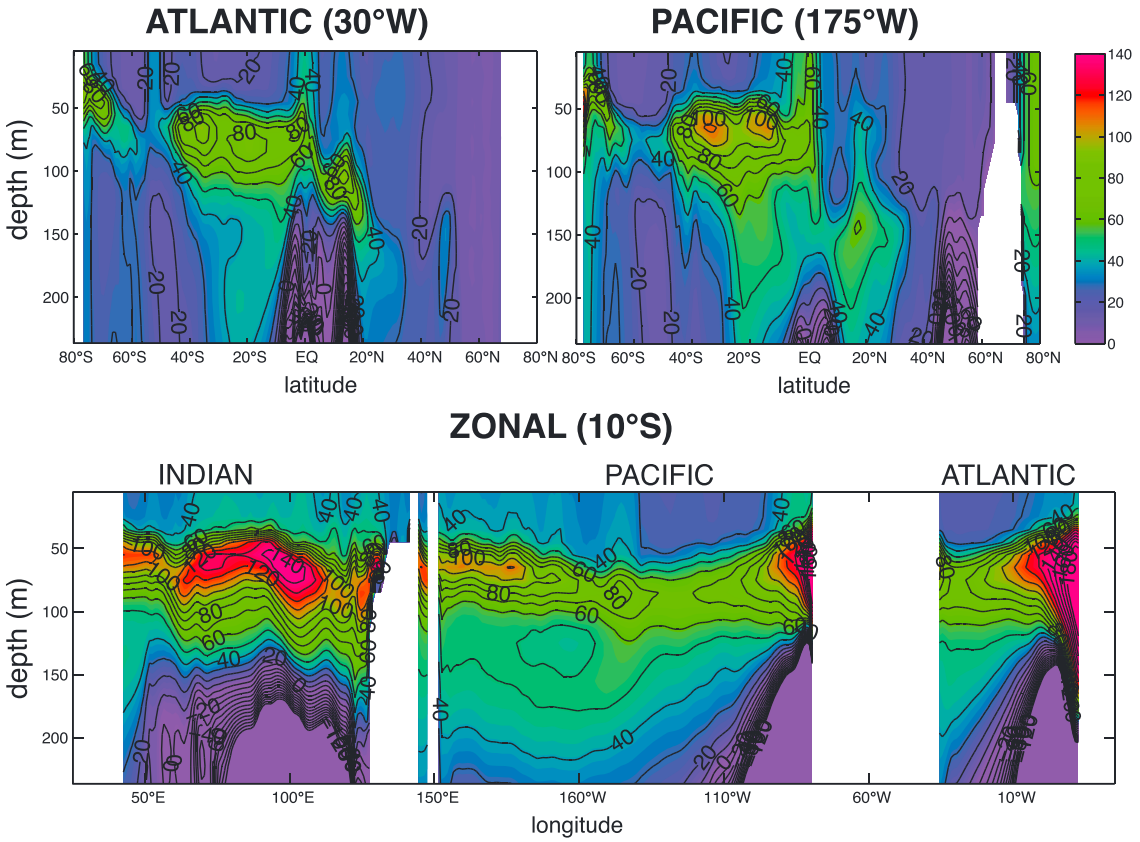

Figure 4. (top) Meridional Atlantic (30°W) and Pacific (175°W) sections and (bottom) zonal section at 10°S of $^{17}\Delta_{dis}$ (ppm) for the normal year simulation after a 200 year spin-up. Both sections are monthly mean $^{17}\Delta_{dis}$ for March, during Southern Hemisphere late summer/early fall when upper thermocline $^{17}\Delta_{dis}$ is highest in the south.

$^{17}\Delta_{dis}$ below −70 ppm (Figure 6). Very few observations of $^{17}\Delta_{dis}$ exist at lower oxygen levels, particularly because the measurement becomes more difficult as the amount of oxygen to analyze decreases. Subsurface measurements in the equatorial Pacific between 170°W and 90°W and between 8°S and 8°N [*Hendricks et al.*, 2005] mostly fall within the same range as our model results for this same region and do include some of the negative values predicted by the model (Figure 6).

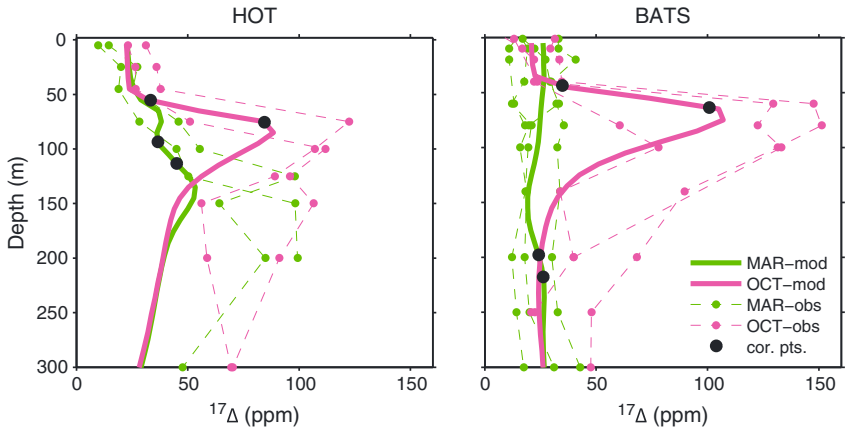

Figure 5. Depth profiles are shown for model (normal year forcing) and observed $^{17}\Delta_{dis}$ profiles from the Hawaii Ocean Timeseries (HOT) and Bermuda Atlantic Time-series (BATS) during early spring and fall. The model underestimates $^{17}\Delta_{dis}$ deeper in the thermocline but is more accurate in the mixed layer and directly below. Observed profiles are shown from several years of observation for each given month, indicating significant interannual variability. Black dots indicate the values at the mixed layer depth and 20 m below that are used for calculating bias correction factors C_{ent} and C_{mix} (from section 5.3).

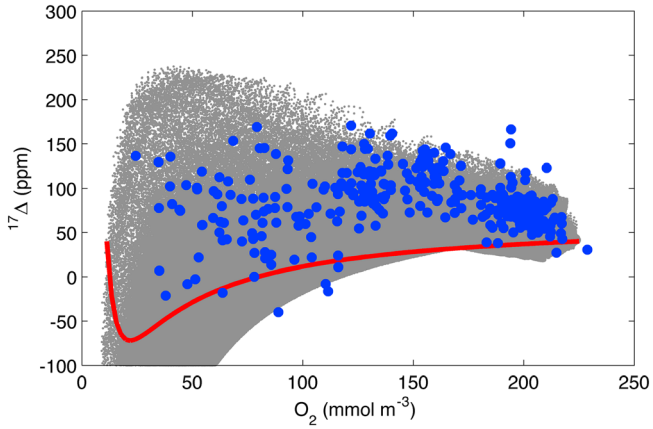

Figure 6. Observations (blue) and model results (grey) for the equatorial Pacific occupy similar parameter space. The red line is a mixing line between two hypothetical water parcels, both with $^{17}\Delta_{dis} = 40$ and compositions of $O_2 = 225$ mmol m^{-3}, $^{18}\delta = 0$ per mil and $O_2 = 11.25$ mmol m^{-3}, $^{18}\delta = 67.1$ per mil, illustrating how the combination of mixing and respiration can create negative $^{17}\Delta_{dis}$.

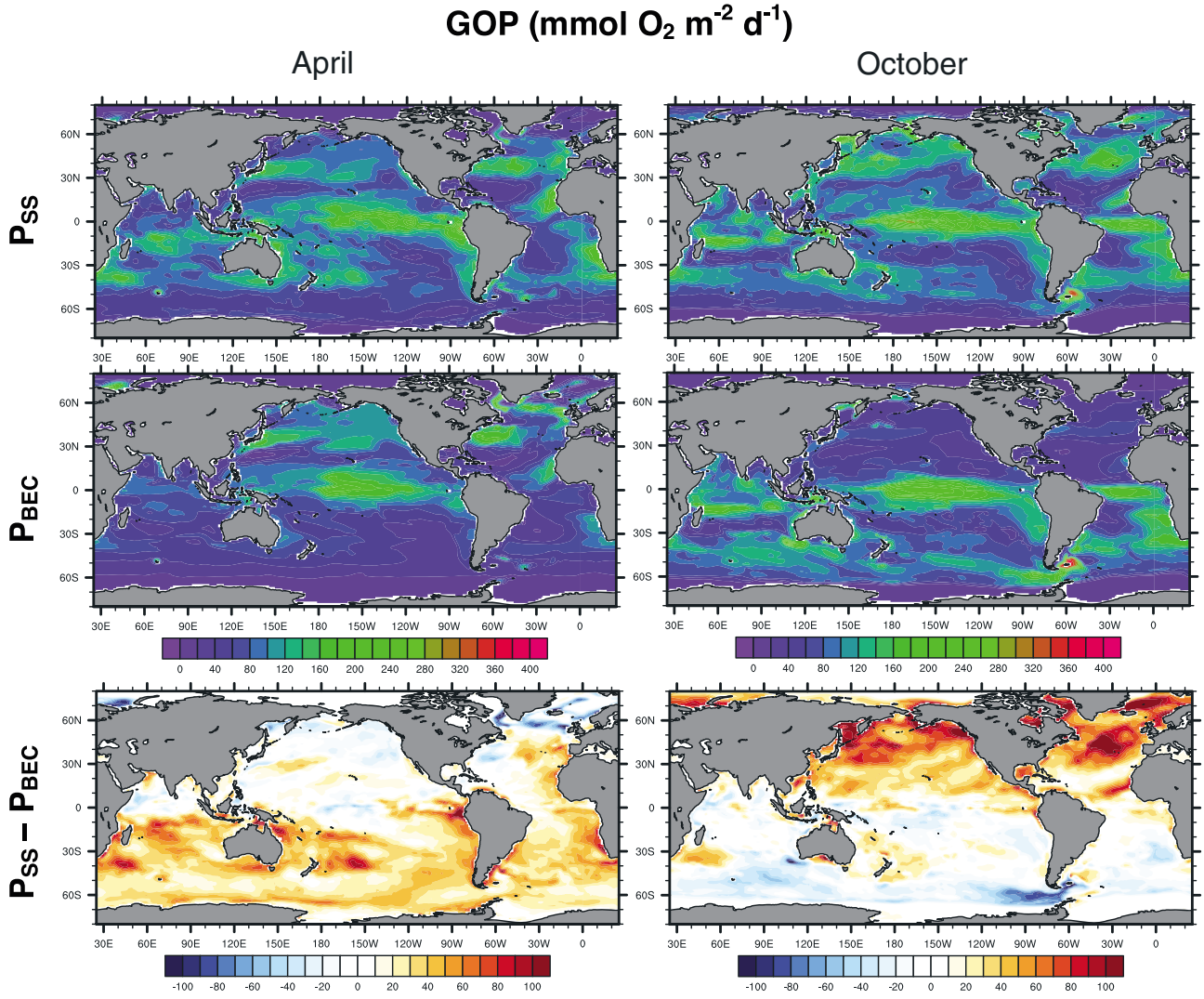

Figure 7. Gross oxygen production (GOP) estimated from triple oxygen isotopes and the steady state equation (P_{SS}) and the actual model GOP (P_{BEC}) are shown for April and October. The bias ($P_{SS} - P_{BEC}$) is shown below.

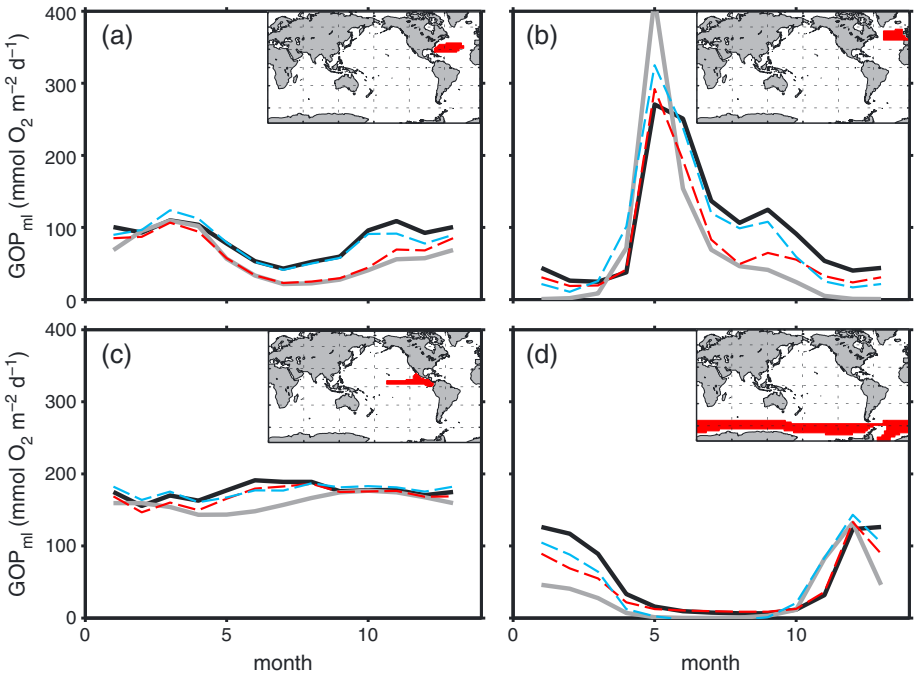

Figure 8. Seasonal cycle of gross oxygen production from the steady state equation, P_{SS} (black) and from model input (grey). The difference between black and grey lines is bias introduced by the steady state assumptions. The dashed line shows GOP when corrected for the nonsteady state term (cyan) and the vertical entrainment/mixing term (red). Results are shown for four example areas in the (a) North Atlantic Subtropical Gyre, (b) subarctic North Atlantic, (c) equatorial Pacific, and (d) Antarctic Southern Ocean. For lower latitude sites, vertical transport is most important, while for higher latitudes, time rate of change becomes more significant.

Deep ocean $^{17}\Delta_{dis}$ may hold interesting tracer information as well, but we do not address the topic in this paper because we estimate that on the order of a 10,000 year spin-up would be needed for the deep ocean to reach equilibrium. Furthermore, $^{17}\Delta_{dis}$ observations for the deep ocean are extremely limited. Due to the nonlinear effect described for the thermocline, we recommend that future studies of $^{17}\Delta_{dis}$ in low oxygen and deep ocean regimes adopt the $^{17}O_{xs}$ definition (equation (9)) because it is conservative with respect to mixing.

5. Results and Discussion: Model Evaluation of Productivity Equations

5.1. Steady State Equation

Model results were applied to diagnose the impact of simplifying equation (2) to the steady state form (equation (4)) when calculating GOP. When referring to the steady state approximation, we use the notation GOP_{SS}. Within the model framework "true" GOP rates (GOP_{BEC}) are known and calculated from summing BEC model organism photosynthetic rates. A comparison of GOP_{SS} and GOP_{BEC} provides an internal consistency test of the degree of bias introduced by the assumptions used to formulate equation (4). Comparisons were made to evaluate both spatial (Figure 7) and temporal (Figure 8) bias patterns. To first order the steady state method reproduces spatial patterns observed in GOP_{BEC} (Figure 7). However, the steady state approximations introduce significant biases in many regions and seasons. Results show that over much of the ocean GOP_{SS} overestimates GOP_{BEC}. Globally averaged, applying a steady state equation to model TOI output results in a GOP_{SS} that is 29% higher than GOP_{BEC}. The largest overestimation occurs during autumn in both Northern and Southern hemispheres, when the overestimation is 62% on average. Spring bloom conditions at higher latitudes are an exception where GOP_{SS} underestimates GOP_{BEC}. For example, in the subarctic North Atlantic province, the springtime underestimation averaged 37% for April and May.

5.2. Corrections for a Dynamic Ocean

Understanding the underlying causes of discrepancies between GOP_{SS} and GOP_{BEC} requires a close evaluation of the approximations and assumptions used to formulate the steady state equation. The degree to which these approximations hold clearly depends on the oceanographic and biological conditions to which they

are applied. The steady state approximation assumes that (1) the time rate of change of $^{17}\Delta_{dis}$ is small and can be neglected and (2) that fluxes of $^{17}\Delta_{dis}$ due to advection and mixing also can be neglected. We assess these terms in the climatological NYF model run to evaluate where and when tracer time rate of change and transport fluxes are large relative to biological terms. In equation (3) the time rate of change term can be broadened to include changes due to transport in addition to biology and gas exchange such that GOP (denoted P in equations) can be estimated as follows:

$$P = \frac{k[O_2]_{eq} A_{eq} + z_{ml}[O_2]\left(\frac{\partial(^{17}\Delta_{dis})}{\partial t} - \left[\frac{\partial(^{17}\Delta_{dis})}{\partial t}\right]_{\psi}\right)}{A_P} \quad (11)$$

where the subscript "ψ" refers to the net effect of ocean physics on the tracer value. The transport term can be further divided into contribution of horizontal advective and diffusive terms, and vertical advective and diffusive terms. Convection (and thus entrainment) is captured within the vertical diffusive term.

Over large regions of the open ocean (Figure 9) we find that advection results in minimal biases in estimating GOP. Advection was important primarily in western boundary currents, isolated regions of the Southern Ocean, and near the equator. This interpretation is to some degree limited by the spatial resolution (~1°) of our model, which does not fully represent mesoscale and submesoscale dynamics. However, our results suggest that a field program averaging a number of observations of spatial scales similar to our model resolution (order of 100 km) will not face significant advective biases in most regions.

We find that the vertical diffusive term is the dominant factor influencing the circulation term of equation (11). While individual advective terms, such as vertical flux and meridional advective divergence can be significant, they tend to balance each other (Figure 9), while the vertical diffusive term accounts for the majority of the circulation bias between GOP_{SS} and GOP_{BEC} (Figure 9). For example, vertical advection increases $^{17}\Delta_{dis}$ during equatorial upwelling due to high subsurface values, but a latitudinal gradient and divergent poleward surface flow cause a tightly coupled compensatory decrease. Vertical mixing/entrainment has the largest impact during late summer and fall in midlatitudes (Figure 9).

The time rate of change of $^{17}\Delta_{dis}$ also has a considerable impact (Figure 9), particularly in higher-latitude areas of high productivity. A similar effect has been observed in a modeling study of the O_2/Ar net community production tracer in the Southern Ocean [*Jonsson et al.*, 2013]. In these high-latitude areas, the time rate of change term can correct for the fact that GOP_{SS} lags behind GOP_{BEC} due to the approximately monthly air-sea time scale for dissolved equilibration. During spring, when $^{17}\Delta_{dis}$ is increasing most rapidly, GOP_{SS} underestimates GOP_{BEC}. During fall, the opposite is the case and GOP_{SS} overestimates GOP_{BEC} (Figure 8). Globally averaged, the absolute value of time rate of change bias was 48% of the magnitude of vertical mixing/entrainment bias.

5.3. Strategies for the Field

We propose a strategy for estimating the bias due to entrainment and vertical mixing based on mixed layer depth history and an additional measure of the TOI composition from 20 m below the mixed layer (z_{deep}). An offset of 20 m from z_{ml} was chosen to be representative of conditions in the seasonal thermocline as well as being far enough removed from z_{ml} to estimate the sub–mixed layer gradient (Figure 5). As mixed layer history is now obtainable from Argo profiling float data and data assimilating models [*Chassignet et al.*, 2007; *Hosoda et al.*, 2010; *Schmidtko et al.*, 2013] and only a single additional sampling is required, our approach is tenable for field programs. To estimate seasonal entrainment, we make the simplifications of assuming a constant rate of mixed layer deepening and a two-layer system in which the sub–mixed layer has the composition measured at z_{deep}. In the supporting information we derive the full equations for correction factors for entrainment (C_{ent}) and mixing (C_{mix}) which can be approximated as follows:

$$C_{ent} \approx \frac{\partial z_{ml}}{dt}\left([O_2]_{deep}{}^{17}\Delta_{deep} - [O_2]_{ml}{}^{17}\Delta_{ml}\right) \quad (12)$$

and

$$C_{mix} \approx \frac{K_z}{z_{deep} - z_{ml}}\left([O_2]_{deep}{}^{17}\Delta_{deep} - [O_2]_{ml}{}^{17}\Delta_{ml}\right) \quad (13)$$

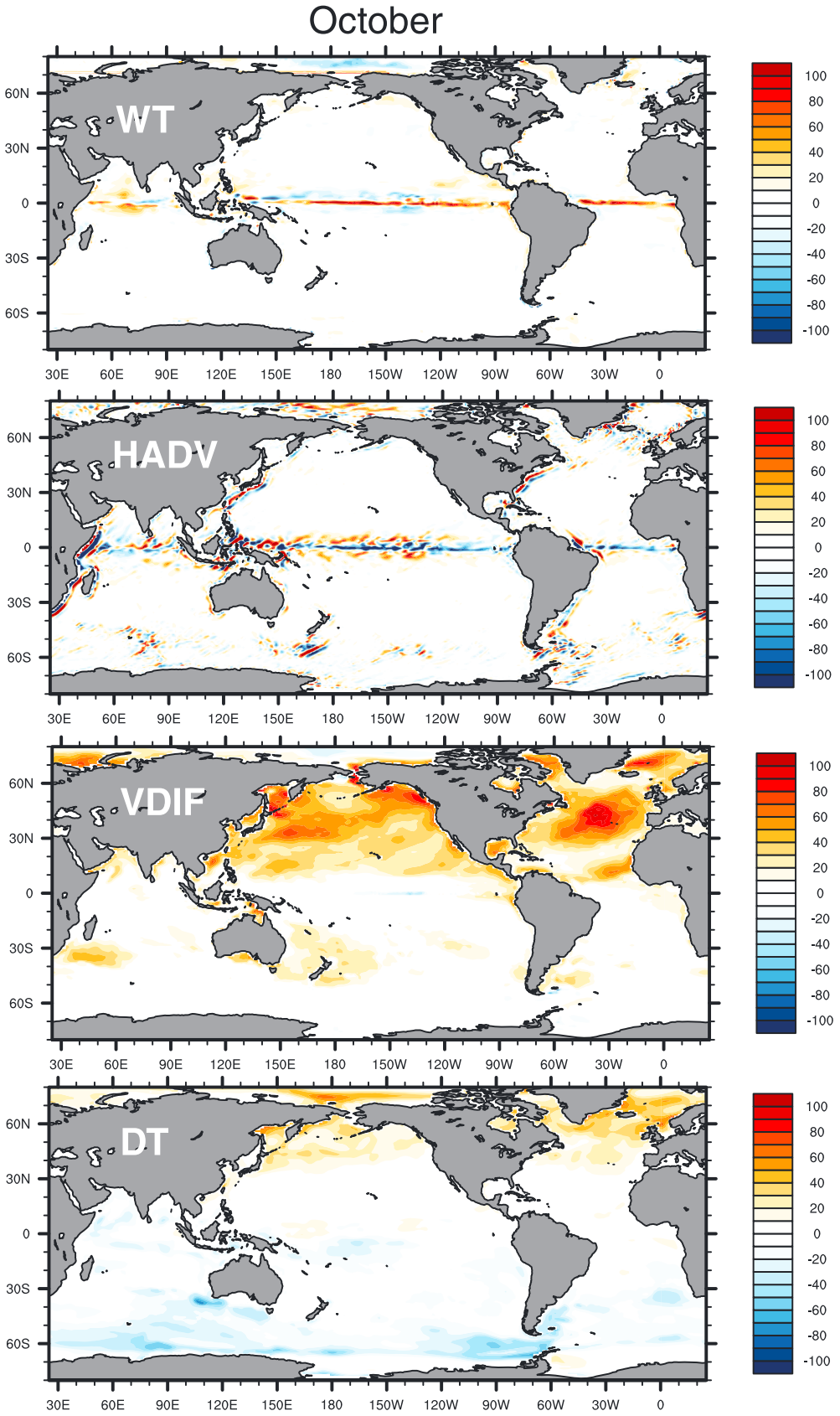

Figure 9

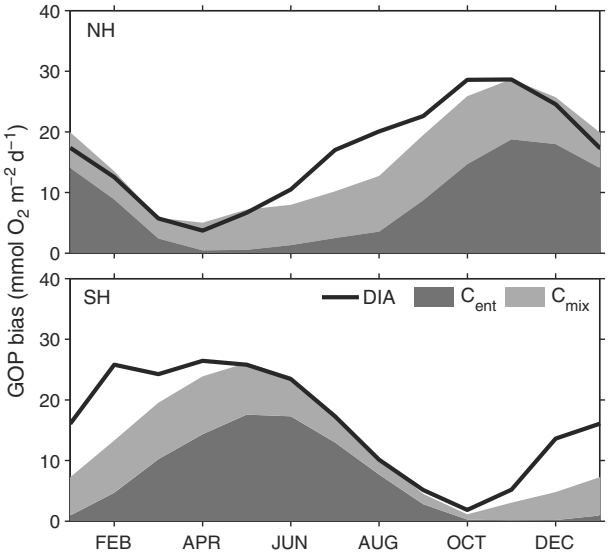

Figure 10. The solid black line indicates total GOP bias due to diapycnal mixing and entrainment (DIA) in the model. The correction factor for entrainment C_{ent} is shaded in dark grey while the correction factor for mixing, C_{mix}, is represented by the light grey area. Panels show average values for the (top) Northern and (bottom) Southern Hemispheres. The correction factors C_{ent} and C_{mix} are most accurate in fall and winter but underestimate diapycnal biases in the summer.

where the K_z is the coefficient for vertical diffusion and subscripts "ml" and "deep" indicated properties measured in the mixed layer and 20 m below, respectively. Correction terms can be applied subtracting the term from the left side of equation (3) (i.e., $z_{ml}[O_2]\frac{d\left({}^{17}\Delta_{,dis}\right)}{dt} - C = P_{ml}A_P - k[O_2]_{eq}A_{eq}$). The full equations ((S7) and (S8)) in the supporting information should preferably be used, as error from the approximations increases as ${}^{18}\delta$ deviates from zero. We chose a value of $K_z = 2\times10^{-4}\,m^2\,s^{-1}$ which is significantly larger than background diffusivity because surface-forced mixing penetrates into the upper thermocline, enhancing effective vertical diffusivity [*Large et al.*, 1994]. Mixed layer depth changes are calculated from monthly mean model output. The above equations have a range of limitations, including the degree to which ${}^{17}\Delta_{deep}$ is representative of entrained water that mixed layer depth does not deepen at a constant rate and that K_z is variable in time and space and seldom constrained. The performance of C_{ent} and C_{mix} is evaluated in the model framework by synthetically sampling model data (Figure 10). While available model diagnostics only provides the total effect of vertical bias, we examine how well the sum of the two correction terms accounts for the total vertical bias. Overall, C_{ent} and C_{mix} accounted for 86% of the model vertical bias. Annually and spatially averaged, C_{ent} was 7.6 mmol $O_2\,m^2\,d^{-1}$ and C_{mix} was 6.4 mmol $O_2\,m^2\,d^{-1}$ although C_{ent} was much more seasonal (Figure 10). C_{mix} tends to be larger over large low-latitude areas while C_{ent} dominates during fall entrainment at middle and high latitudes (see supporting information). For example, in October in the Northern Hemisphere, C_{ent} was 18.8 mmol $O_2\,m^2\,d^{-1}$ and C_{mix} was 9.9 mmol O_2 $m^2\,d^{-1}$. During summer, the sum of the correction terms underestimates the actual model vertical bias and the simple formulations for C_{ent} and C_{mix} appear to break down (Figure 10). This may be due to processes such as high frequency variability in mixed layer depth, spatiotemporal variability in the effective K_z, and limitations in the ability of a single deep measurement to quantify actual sub–mixed layer gradients. Despite these shortcomings, the bias correction, particularly C_{ent} when applied to fall entrainment in temperate environments does an admirable job at estimating the primary source of bias in GOP_{SS}.

Figure 9. Nonsteady state correction terms shown for October of normal year forcing simulation. The influence of vertical advection (WT), horizontal advection (HADV), vertical mixing/entrainment (VDIF), and time rate of change (DT) are shown in GOP units (mmol $O_2\,m^{-2}\,d^{-1}$). The influence of horizontal diffusion was much smaller than other terms and is not shown. Red/orange areas correspond to amount that the given process causes GOP_{SS} to overestimate GOP_{MOD}, while blue colors are areas of GOP_{SS} underestimation. Note that in the DT panel, positive values represent regions where ${}^{17}\Delta_{dis}$ is decreasing with time. In equatorial regions, the effect of upwelling (WT) is largely balanced by compensatory equatorial divergence (HADV).

6. Summary and Conclusions

In simulating $^{17}\Delta_{dis}$ we found that we were able to reproduce major observed patterns of mixed layer $^{17}\Delta_{dis}$ in CESM. Globally, simulations for normal year forced and interannually forced simulations had mean biases of −5.2 ppm and −4.8 ppm, respectively. Regionally, model performance was best in the Pacific and weakest in the Southern Ocean and in coastal regions. Below the mixed layer, subsurface maxima in midlatitudes and low latitudes were somewhat lower than observations, likely due to insufficient photosynthesis at depth in the model. In the thermocline, particularly areas with very low oxygen, we identified that nonlinear mixing effects of the $^{17}\Delta$ tracer system can result in negative $^{17}\Delta_{dis}$ values. While TOI measurements are difficult when oxygen is below roughly 20% of saturation, existing data from the equatorial Pacific [*Hendricks et al.*, 2005] support the presence of negative values predicted by the model (Figure 6).

Modeling TOI in CESM leads to several results that can be applied to improving field-based estimates of gross oxygen production. Vertical mixing/entrainment was the largest sources of biases introduced when applying the steady state equation for GOP_{SS} with the time rate of change of tracer values also a significant source of bias. Spatially, entrainment/mixing dominated in low and temperate latitudes where high subsurface $^{17}\Delta_{dis}$ accumulates and bias from time rate of change increased in importance at higher latitudes in regions with large seasonality in primary production. The seasonal cycle of these two processes differs as well. Entrainment-/mixing-induced biases tend to be highest in late summer and fall (when mixed layers tend to deepen) and lower during spring and winter. Entrainment/mixing almost never results in a negative bias (underestimation of GOP). The time rate of change bias tends to cause a negative bias in spring and periods of intense productivity, which is then balanced by a positive bias through summer and fall. Thus, for the annual mean, entrainment/mixing is a more significant source of bias than is time rate of change.

We propose an approach to correct for entrainment and mixing bias in the field based on mixed layer depth history and an additional TOI measurement from 20 m below the mixed layer. When applied to model data, these equations account for 86% of bias from vertical processes do an excellent job of estimating bias during autumn but significantly underestimate bias during summer.

Acknowledgments
We acknowledge support from Center for Microbial Oceanography Research and Education (CMORE) (NSF EF-0424599) and NOAA Climate Program Office (NA 100AR4310093). We also would like to thank those who collected, analyzed, shared, and published original TOI and ancillary data used for this study.

References

Angert, A., S. Rachmilevitch, E. Barkan, and B. Luz (2003), Effects of photorespiration, the cytochrome pathway, and the alternative pathway on the triple isotopic composition of atmospheric O_2, *Global Biogeochem. Cycles*, *17*(1), 1030, doi:10.1029/2002GB001933.

Benson, B. B., and D. Krause (1984), The concentration and isotopic fractionation of oxygen dissolved in freshwater and seawater in equilibrium with the atmosphere, *Limnol. Oceanogr.*, *29*(3), 620–632.

Castro-Morales, K., N. Cassar, and J. Kaiser (2012), Biological production in the Bellingshausen Sea from oxygen-to-argon ratios and oxygen triple isotopes, *Biogeosci. Discuss.*, *9*(11), 16,033–16,085, doi:10.5194/bgd-9-16033-2012.

Chassignet, E. P., H. E. Hurlburt, O. M. Smedstad, G. R. Halliwell, P. J. Hogan, A. J. Wallcraft, R. Baraille, and R. Bleck (2007), The HYCOM (HYbrid Coordinate Ocean Model) data assimilative system, *J. Mar. Syst.*, *65*(1–4), 60–83, doi:10.1016/j.jmarsys.2005.09.016.

Danabasoglu, G., S. C. Bates, B. P. Briegleb, S. R. Jayne, M. Jochum, W. G. Large, S. Peacock, and S. G. Yeager (2012), The CCSM4 ocean component, *J. Clim.*, *25*(5), 1361–1389, doi:10.1175/JCLI-D-11-00091.1.

Doney, S. C., K. Lindsay, I. Fung, and J. John (2006), Natural variability in a stable, 1000 year global coupled climate-carbon cycle simulation, *J. Clim.*, *19*, 3033–3054, doi:10.1175/JCLI3783.1.

Doney, S. C., S. Yeager, G. Danabasoglu, W. G. Large, and J. C. McWilliams (2007), Mechanisms governing interannual variability of upper-ocean temperature in a global ocean hindcast simulation, *J. Phys. Ocean.*, *37*(7), 1918–1938, doi:10.1175/JPO3089.1.

Doney, S. C., I. Lima, J. K. Moore, K. Lindsay, M. J. Behrenfeld, T. K. Westberry, N. Mahowald, D. M. Glover, and T. Takahashi (2009), Skill metrics for confronting global upper ocean ecosystem-biogeochemistry models against field and remote sensing data, *J. Mar. Syst.*, *76*(1–2), 95–112, doi:10.1016/j.jmarsys.2008.05.015.

Eiler, A. (2006), Evidence for the ubiquity of mixotrophic bacteria in the upper ocean: Implications and consequences, *Appl. Environ. Microbiol.*, *72*(12), 7431–7437, doi:10.1128/AEM.01559-06.

Garcia, H. E., and L. I. Gordon (1992), Oxygen solubility in seawater: Better fitting equations, *Limnol. Oceanogr.*, *37*(6), 1307–1312, doi:10.4319/lo.1992.37.6.1307.

Gent, P. R., et al. (2011), The Community Climate System Model version 4, *J. Clim.*, *24*(19), 4973–4991, doi:10.1175/2011JCLI4083.1.

Halsey, K. H., A. J. Milligan, and M. J. Behrenfeld (2010), Physiological optimization underlies growth rate-independent chlorophyll-specific gross and net primary production, *Photosynth. Res.*, *103*(2), 125–137, doi:10.1007/s11120-009-9526-z.

Hamme, R. C., et al. (2012), Dissolved O_2/Ar and other methods reveal rapid changes in productivity during a Lagrangian experiment in the Southern Ocean, *J. Geophys. Res.*, *117*, C00F12, doi:10.1029/2011JC007046.

Helman, Y., E. Barkan, D. Eisenstadt, B. Luz, and A. Kaplan (2005), Fractionation of the three stable oxygen isotopes by oxygen-producing and oxygen-consuming reactions in photosynthetic organisms, *Plant Physiol.*, *138*(4), 2292–2298, doi:10.1104/pp.105.063768.

Hendricks, M. B., M. L. Bender, B. A. Barnett, P. Strutton, and F. P. Chavez (2005), Triple oxygen isotope composition of dissolved O_2 in the equatorial Pacific: A tracer of mixing, production, and respiration, *J. Geophys. Res.*, *110*, C12021, doi:10.1029/2004JC002735.

Hosoda, S., T. Ohira, K. Sato, and T. Suga (2010), Improved description of global mixed-layer depth using Argo profiling floats, *J. Oceanogr.*, *66*(6), 773–787, doi:10.1007/s10872-010-0063-3.

Huang, K., H. Ducklow, M. Vernet, N. Cassar, and M. L. Bender (2012), Export production and its regulating factors in the West Antarctica Peninsula region of the Southern Ocean, *Global Biogeochem. Cycles*, *26*, GB2005, doi:10.1029/2010GB004028.

Johnson, Z. I., E. R. Zinser, A. Coe, N. P. McNulty, E. M. S. Woodward, and S. W. Chisholm (2006), Niche partitioning among Prochlorococcus ecotypes along ocean-scale environmental gradients, *Science*, *311*(5768), 1737–1740, doi:10.1126/science.1118052.

Jonsson, B. F., S. C. Doney, J. Dunne, and M. Bender (2013), Evaluation of the Southern Ocean O2/Ar-based NCP estimates in a model framework, *J. Geophys. Res. Biogeosci.*, *118*, 385–399, doi:10.1002/jgrg.20032.

Juranek, L. W., and P. D. Quay (2010), Basin-wide photosynthetic production rates in the subtropical and tropical Pacific Ocean determined from dissolved oxygen isotope ratio measurements, *Global Biogeochem. Cycles*, *24*, GB2006, doi:10.1029/2009GB003492.

Juranek, L. W., and P. D. Quay (2013), Using triple isotopes of dissolved oxygen to evaluate global marine productivity, *Annu. Rev. Mar. Sci.*, *5*(1), 503–524, doi:10.1146/annurev-marine-121211-172430.

Juranek, L. W., P. D. Quay, R. A. Feely, D. Lockwood, D. M. Karl, and M. J. Church (2012), Biological production in the NE Pacific and its influence on air-sea CO2 flux: Evidence from dissolved oxygen isotopes and O2/Ar, *J. Geophys. Res.*, *117*, C05022, doi:10.1029/2011JC007450.

Kaiser, J. (2011), Technical note: Consistent calculation of aquatic gross production from oxygen triple isotope measurements, *Biogeosciences*, *8*(7), 1793–1811, doi:10.5194/bg-8-1793-2011.

Knox, M., P. D. Quay, and D. Wilbur (1992), Kinetic isotopic fractionation during air-water gas transfer of O_2, N_2, CH_4, and H_2, *J. Geophys. Res.*, *97*(C12), 20,335–20,343, doi:10.1029/92JC00949.

Lämmerzahl, P., T. Röckmann, C. A. M. Brenninkmeijer, D. Krankowsky, and K. Mauersberger (2002), Oxygen isotope composition of stratospheric carbon dioxide, *Geophys. Res. Lett.*, *29*(12), 1582, doi:10.1029/2001GL014343.

Large, W. G., J. C. McWilliams, and S. C. Doney (1994), Oceanic vertical mixing: A review and a model with a nonlocal boundary layer parameterization, *Rev. Geophys.*, *32*(4), 363–403, doi:10.1029/94RG01872.

Laws, E. A., M. R. Landry, R. T. Barber, L. Campbell, M.-L. Dickson, and J. Marra (2000), Carbon cycling in primary production bottle incubations: Inferences from grazing experiments and photosynthetic studies using ^{14}C and ^{18}O in the Arabian Sea, *Deep Sea Res., Part II*, *47*(7–8), 1339–1352, doi:10.1016/S0967-0645(99)00146-0.

Letelier, R. M., D. M. Karl, M. R. Abbott, and R. R. Bidigare (2004), Light driven seasonal patterns of chlorophyll and nitrate in the lower euphotic zone of the North Pacific Subtropical Gyre, *Limnol. Oceanogr.*, *49*, 508–519.

Levine, N. M., M. L. Bender, and S. C. Doney (2009), The $\delta^{18}O$ of dissolved O_2 as a tracer of mixing and respiration in the mesopelagic ocean, *Global Biogeochem. Cycles*, *23*, GB1006, doi:10.1029/2007GB003162.

Long, M. C., K. Lindsay, S. Peacock, J. K. Moore, and S. C. Doney (2013), Twentieth-century oceanic carbon uptake and storage in CESM1(BGC), *J. Clim.*, *26*, 6775–6800, doi:10.1175/JCLI-D-12-00184.1.

Longhurst, A. R. (2006), *Ecological Geography of the Sea*, 2nd ed., Academic Press, San Diego, Calif.

Loose, B., W. R. McGillis, P. Schlosser, D. Perovich, and T. Takahashi (2009), Effects of freezing, growth, and ice cover on gas transport processes in laboratory seawater experiments, *Geophys. Res. Lett.*, *36*, L05603, doi:10.1029/2008GL036318.

Luz, B., and E. Barkan (2000), Assessment of oceanic productivity with the triple-isotope composition of dissolved oxygen, *Science*, *288*(5473), 2028–2031, doi:10.1126/science.288.5473.2028.

Luz, B., and E. Barkan (2005), The isotopic ratios $^{17}O/^{16}O$ and $^{18}O/^{16}O$ in molecular oxygen and their significance in biogeochemistry, *Geochim. Cosmochim. Acta*, *69*(5), 1099–1110, doi:10.1016/j.gca.2004.09.001.

Luz, B., and E. Barkan (2009), Net and gross oxygen production from O_2/Ar, $^{17}O/^{16}O$ and $^{18}O/^{16}O$ ratios, *Aquat. Microb. Ecol.*, *56*, 133–145, doi:10.3354/ame01296.

Luz, B., and E. Barkan (2011), Proper estimation of marine gross O_2 production with $^{17}O/^{16}O$ and $^{18}O/^{16}O$ ratios of dissolved O_2, *Geophys. Res. Lett*, *38*, L9606, doi:10.1029/2011GL049138.

Marra, J. (2002), Approaches to the measurement of plankton production, in *Phytoplankton Productivity: Carbon Assimilation in Marine and Freshwater Ecosystems*, edited by P. J. l. B. Williams, D. N. Thomas, and C. S. Reynolds, chap. 4, Blackwell Science Ltd., Oxford, U. K., doi:10.1002/9780470995204.ch4.

Moore, J. K., S. C. Doney, and K. Lindsay (2004), Upper ocean ecosystem dynamics and iron cycling in a global three-dimensional model, *Global Biogeochem. Cycles*, *18*, GB4028, doi:10.1029/2004GB002220.

Moore, J. K., K. Lindsay, S. C. Doney, M. C. Long, and K. Misumi (2013), Marine ecosystem dynamics and biogeochemical cycling in the Community Earth System Model [CESM1(BGC)]: Comparison of the 1990s with the 2090s under the RCP4.5 and RCP8.5 scenarios, *J. Clim.*, *26*(23), 9291–9312, doi:10.1175/JCLI-D-12-00566.1.

Muñoz-Marín, M. d. C., I. Luque, M. V. Zubkov, P. G. Hill, J. Diez, and J. M. García-Fernández (2013), Prochlorococcus can use the Pro1404 transporter to take up glucose at nanomolar concentrations in the Atlantic Ocean, *Proc. Natl. Acad. Sci. U.S.A.*, *110*(21), 8597–8602, doi:10.1073/pnas.1221775110.

Munro, D. R., P. D. Quay, L. W. Juranek, and R. Goericke (2013), Biological production rates off the Southern California coast estimated from triple O_2 isotopes and O_2: Ar gas ratios, *Limnol. Oceanogr.*, *58*(4), 1312–1328, doi:10.4319/lo.2013.58.4.1312.

Nicholson, D., R. H. R. Stanley, E. Barkan, D. M. Karl, B. Luz, P. D. Quay, and S. C. Doney (2012), Evaluating triple oxygen isotope estimates of gross primary production at the Hawaii Ocean Time-series and Bermuda Atlantic Time-series Study sites, *J. Geophys. Res.*, *117*, C05012, doi:10.1029/2010JC006856.

Prokopenko, M. G., O. M. Pauluis, J. Granger, and L. Y. Yeung (2011), Exact evaluation of gross photosynthetic production from the oxygen triple-isotope composition of O_2: Implications for the net-to-gross primary production ratios, *Geophys. Res. Lett.*, *38*, L14603, doi:10.1029/2011GL047652.

Quay, P., J. Stutsman, and T. Steinhoff (2012), Primary production and carbon export rates across the subpolar N. Atlantic Ocean basin based on triple oxygen isotope and dissolved O_2 and Ar gas measurements, *Global Biogeochem. Cycles*, *26*, GB2003, doi:10.1029/2010GB004003.

Quay, P. D., D. M. Karl, C. Peacock, and K. M. Bjorkman (2010), Measuring primary production rates in the ocean: Differences between incubation, non-incubation and satellite based methods at Stn ALOHA, *Global Biogeochem. Cycles*, *24*, GB3014, doi:10.1029/2009GB003665.

Reuer, M. K., B. A. Barnett, M. L. Bender, P. G. Falkowski, and M. B. Hendricks (2007), New estimates of Southern Ocean biological production rates from O_2/Ar ratios and the triple isotope composition of O_2, *Deep Sea Res., Part I*, *54*(6), 951–974, doi:10.1016/j.dsr.2007.02.007.

Sarma, V., O. Abe, and T. Saino (2008), Spatial variations in time-integrated plankton metabolic rates in Sagami Bay using triple oxygen isotopes and O_2: Ar ratios, *Limnol. Oceanogr.*, *53*(5), 1776–1783.

Schmidtko, S., G. C. Johnson, and J. M. Lyman (2013), MIMOC: A global monthly isopycnal upper-ocean climatology with mixed layers, *J. Geophys. Res. Oceans*, *118*, 1658–1672, doi:10.1002/jgrc.20122.

Stanley, R. H. R., J. B. Kirkpatrick, N. Cassar, B. Barnett, and M. L. Bender (2010), Net community production and gross primary production rates in the western equatorial Pacific, *Global Biogeochem. Cycles*, *24*, GB4001, doi:10.1029/2009GB003651.

Yeung, L. Y., et al. (2012), Impact of diatom-diazotroph associations on carbon export in the Amazon River plume, *Geophys. Res. Lett.*, *39*, L18609, doi:10.1029/2012GL053356.